ARTICLE IN PRESS

Earthquake Research Advances xxx (xxxx) xxx

Contents lists available at ScienceDirect

Earthquake Research Advances

journal homepage: www.keaipublishing.com/en/journals/earthquake-research-advances

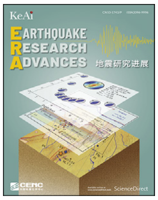

The seismicity in the middle section of the Altyn Tagh Fault system revealed by a dense nodal seismic array

Shi Yao [a,d], Tao Xu [a,c,*], Yingquan Sang [a,b,d], Lingling Ye [b], Tingwei Yang [a,d], Chenglong Wu [a,c], Minghui Zhang [e]

[a] *Key Laboratory of Mineral Resources, Institute of Geology and Geophysics, Chinese Academy of Sciences, Beijing, 100029, China*
[b] *Department of Earth and Space Sciences, Southern University of Science and Technology, Shenzhen, 518055, China*
[c] *Innovation Academy for Earth Science, Chinese Academy of Sciences, Beijing, 100029, China*
[d] *University of Chinese Academy of Sciences, Beijing, 100049, China*
[e] *School of Information Engineering, Shandong University of Aeronautics, Binzhou, 256603, China*

ARTICLE INFO

Keywords:
Altyn Tagh Fault
Machine learning
Seismicity
Dense seismic array

ABSTRACT

The left-lateral Altyn Tagh Fault (ATF) system is the northern boundary of the Qinghai-Xizang Plateau, separating the Tarim Basin and the Qaidam Basin. The middle section of ATF has not recorded any large earthquakes since 1598 AD, so the potential seismic hazard is unclear. We develope an earthquake catalog using continuous waveform data recorded by the Tarim-Altyn-Qaidam dense nodal seismic array from September 17 to November 23, 2021 in the middle section of ATF. With the machine learning-based picker, phase association, location, match and locate workflow, we detecte 233 earthquakes with M_L -1-3, far more than 6 earthquakes in the routine catalog. Combining with focal mechanism solutions and the local fault structure, we find that seismic events are clustered along the ATF with strike-slip focal mechanisms and on the southern secondary faults with thrusting focal mechanisms. This overall seismic activity in the middle section of the ATF might be due to the northeastward transpressional motion of the Qinghai-Xizang Plateau block at the western margin of the Qaidam Basin.

1. Introduction

The left-lateral Altyn Tagh Fault (ATF) system is the northern boundary of the Qinghai-Xizang Plateau, which marks the boundary between the Tarim Basin and the north Qinghai-Xizang Plateau and regulates the far-field effects of the India-Eurasia collision (Molnar and Tapponnier, 1975; Tapponnier et al., 2001; Shen et al., 2001; Yin et al., 2002; Xu et al., 2011). Driven by the northeastward migration of the Qinghai-Xizang Plateau, the slip rate of the western segment of the ATF is approximately 13 mm/year, gradually decreasing to around 0.1 mm/year towards the east, with ~10 mm/a in the middle section (Bendick et al., 2000; Wallace et al., 2004; Zhang et al., 2007; Elliott et al., 2008; Li et al., 2018). Although the ATF lies on the northern margin of the Qinghai-Xizang Plateau and exhibits significant slip rates throughout its main fault segments, no large earthquakes are recorded in the middle section of ATF. Since 1900, there have been no recorded earthquakes larger than M_W 6.5 in the middle section of the ATF, and the most recent earthquake larger than M_W 6 occurred in 1993. The absence of moderate to great earthquakes is peculiar compared to other boundaries of the Qinghai-Xizang Plateau, which have experienced multiple catastrophic earthquakes over the last century (Fig. 1a). For instance, the 1920 M_W 7.9 Haiyuan earthquake occurred along the northeastern margin of the Qinghai-Xizang Plateau (Ou et al., 2020); The 2008 M_W 7.9 Wenchuan earthquake occurred along the southeastern margin of the Qinghai-Xizang Plateau (Shen et al., 2009; Pu et al., 2022); And the 2014 M_W 6.9 Yutian earthquake along the western section of the ATF on the northwestern margin of the Qinghai-Xizang Plateau (Yuan et al., 2021). Large earthquakes primarily occur along the Kunlun Fault and its

---

* Corresponding author. Key Laboratory of Mineral Resources, Institute of Geology and Geophysics, Chinese Academy of Sciences, Beijing, 100029, China.
E-mail address: xutao@mail.iggcas.ac.cn (T. Xu).

Production and Hosting by Elsevier on behalf of KeAi

https://doi.org/10.1016/j.eqrea.2024.100308
Received 31 January 2024; Received in revised form 3 April 2024; Accepted 6 April 2024

Please cite this article as: Yao, S. et al., The seismicity in the middle section of the Altyn Tagh Fault system revealed by a dense nodal seismic array, Earthquake Research Advances, https://doi.org/10.1016/j.eqrea.2024.100308

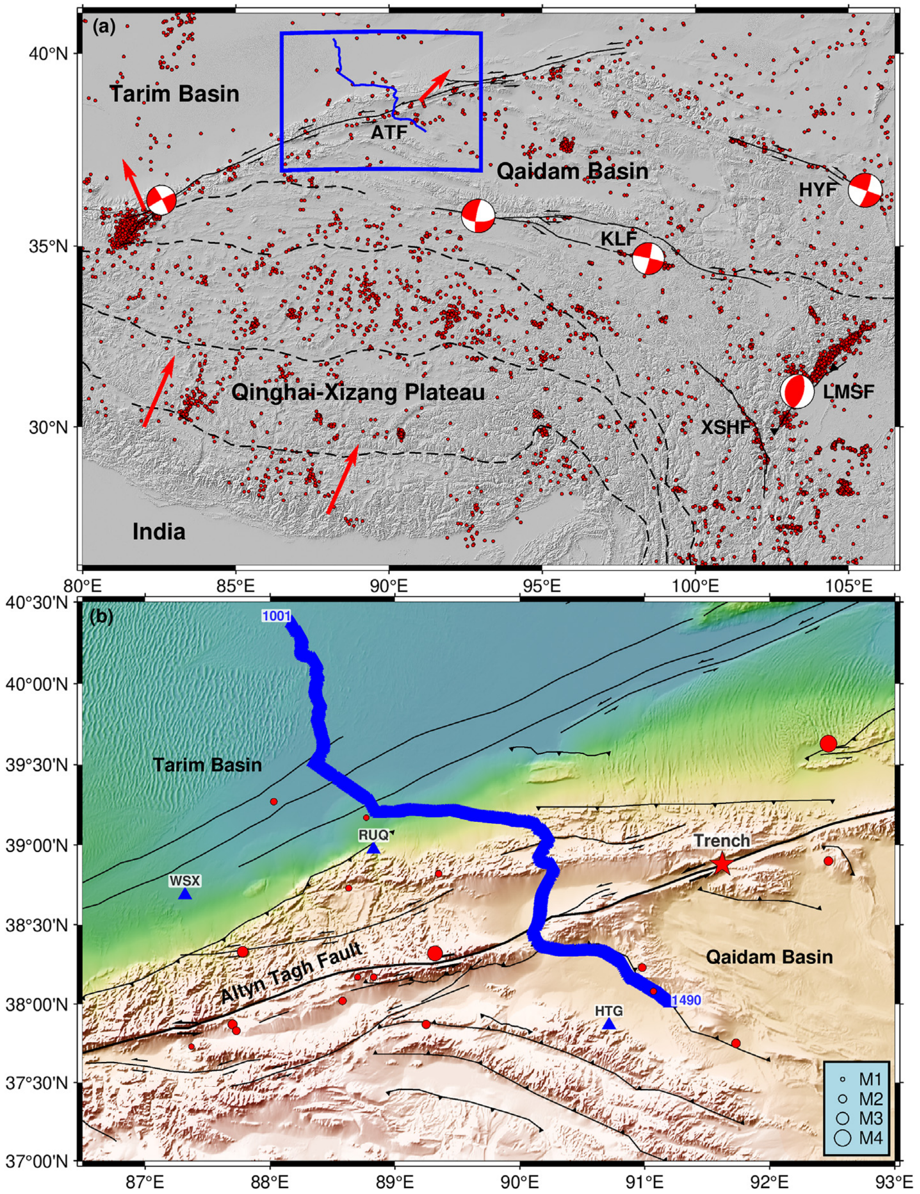

Fig. 1. (a) Tectonic setting of the Qinghai-Xizang Plateau. The dark red dots denote the earthquakes with $M_L > 3$ from 2007 to 2022. The focal mechanisms show earthquakes ($M > 7.0$) in the Qinghai-Xizang Plateau and its margins. The solid black lines show main faults, and black dashed lines mark block boundaries. Red arrows show the average GPS velocity field relative to the Qinghai-Xizang Plateau (Wang et al., 2020). (b) Tectonic setting of the middle section of the Altyn Tagh Fault and location of the dense seismic array (corresponding to the blue rectangle in Fig. 1a). Blue triangles indicate the seismic stations. The red dots denote the earthquakes (September 17 to November 23, 2021). The red stars represent the locations of the paleoseismic trench (Yuan et al., 2018). Fault data are from the Active Tectonics Map of China (Deng, 2007) and the HimaTibetMap database (Styron et al., 2010). ATF: Altyn Tagh Fault. HYF: Haiyuan Fault. XSHF: Xianshuihe Fault. LMSF: Longmenshan Fault. KLF: Kunlun Fault.

associated branches, located south of the Qinghai Basin, include the 2001 M_W 7.8 Kunlun earthquake (Robinson et al., 2006) and the 2021 M_W 7.4 Madoi earthquake (Wang et al., 2021). The microseismicity in the middle section of the ATF is also weak (Fig. 1a).

Given its considerable slip rate, the potential seismic hazard in the middle section of the ATF remains a concern. The paleoseismic study demonstrated that the most recent great earthquake in this section occurred in 1598 AD (1491–1741) with a magnitude up to M_W 7.8–8.1 based on the estimated surface displacement and rupture length (Yuan et al., 2018). With the slip rate of ~10 mm/a, the maximum slip deficit is 3.3–4.6 m. Based on dense Global Positioning System (GPS) observations, Li et al. (2018) found that the locking depth reaches 5–15 km and 15–20 km in the western and middle section of the ATF, respectively, and the accumulated strain in these sections suggests the potential for earthquakes ranging from M_W 7.6 to 7.8.

High-precision earthquake catalogs offer insight into the intricate details of seismic fault structures, thereby facilitating a more accurate assessment of seismic hazard (Waldhauser and Ellsworth, 2002; Yang et al., 2009; Shelly et al., 2016; Zhou et al., 2022b). The detection and location of seismic events are crucial for constructing high-precision earthquake catalogs, primarily employing waveform-based methods and pick-based methods. The waveform-based methods, primarily based on the delay-and-sum theory, can construct earthquake catalogs in a single step, typically rely on waveform energy or coherence to detect, associate, and locate earthquakes, possessing detection capability for small-magnitude events (Stewart, 1977; Shelly et al., 2007; Peng and Zhao, 2009; Zhang and Wen, 2015). However, they often use grid-search methods to perform stacking or correlation computations at each grid point, resulting in high computational costs. In contrast, pick-based methods are the preferred solution due to their higher computational efficiency. Typically, these methods pick the seismic phases first and then perform phase association and earthquake location based on picks. Picking of seismic phases is crucial for such methods. Recently, machine learning (ML)-based pickers, along with the establishment of large artificial datasets, have significantly improved the efficiency of picking while maintaining high accuracy (Mousavi et al., 2019, 2020; Wang et al., 2019; Zhu and Beroza, 2019; Zhao et al., 2022).

With the development of phase pickers and datasets, some researchers have integrated high-precision earthquake catalog construction workflow based on continuous waveform data using existing phase picking, phase association, and earthquake location methods, such as PALM (Zhou et al., 2022a), LOC-FLOW (M Zhang et al., 2022), ESPRH

(Wu et al., 2022) and QuakeFlow (Zhu et al., 2023). These workflows have been widely used in foreshocks and aftershocks (Liu et al., 2020; Zhou et al., 2021; Su et al., 2021; Zhao et al., 2021; Wen et al., 2022; Zuo et al., 2023), regional seismicity (Daniels and Peng, 2023; K Wang et al., 2023), induced earthquakes (Park et al., 2020; R Wang et al., 2023), magmatic activities (Wilding et al., 2023) and structures in subduction/collision zones (Ammirati et al., 2022; Jiang et al., 2022).

In this study, we construct a high-precision earthquake catalog in the middle section of the ATF using continuous waveform from a temporary dense nodal seismic array and permanent stations. Our workflow involves phase picking, event association, earthquake location, and magnitude computation (M_L), following the LOC-FLOW developed by Zhang et al. (2022).

2. Data and method

2.1. Data and preprocess

We use the data from the Tarim-Altyn-Qaidam dense nodal seismic array, part of the Second Qinghai-Xizang Plateau Scientific Expedition and Research Program, from September 17 to November 23, 2021, which consisted of 483 short-period three-component portable seismographs (EPS-5S and EPS-20S) with an average station interval of ~1 km (Xie et al., 2023; Wu et al., 2024). To improve the precision of earthquake location, we also integrated data from 3 nearby permanent broadband seismic stations (Fig. 1b).

Short-period seismometers have been widely used in recent years for detailed crustal structure investigations at regional scales benefiting from their simple operation and low cost. Compared to broadband seismometers, they may exhibit slightly lower quality, particularly issues such as posture, clock drift, and component azimuths. We conduct quality analysis and data selection, following preprocessing methods for ocean bottom seismometers (Yang et al., 2023, Fig. 2):

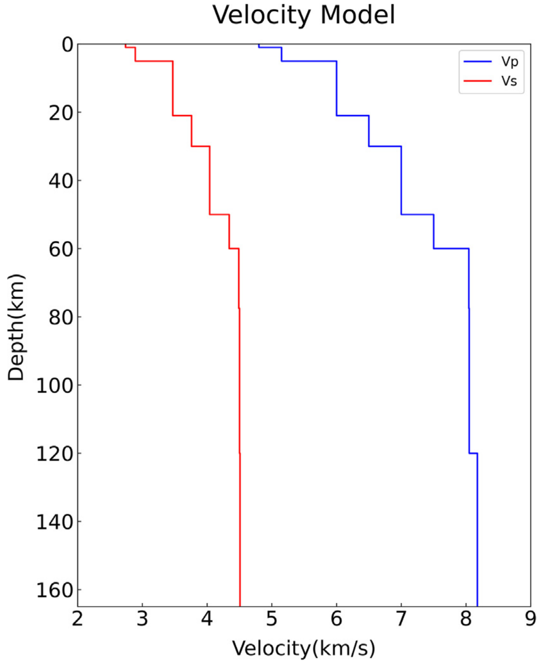

Fig. 3. The 1D velocity model for catalog construction.

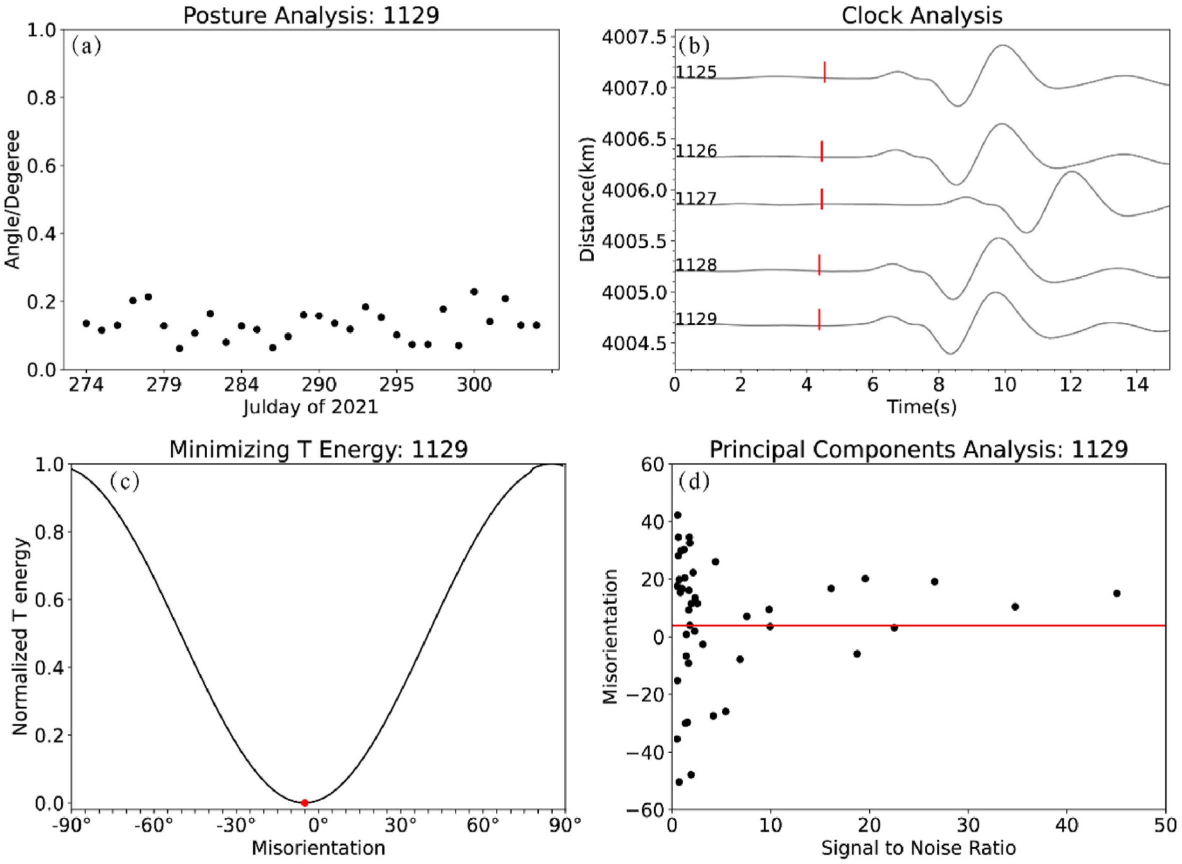

Fig. 2. An example of quality analysis of a seismometer (station 1129). (a) Posture analysis (the black dots denote the tilt angle). (b) Clock analysis of stations 1125–1129 (red solid bars indicate the P arrivals). (c) Component azimuth based on the SNR-weighted-multi-event method (the red dot indicates the component azimuth). (d) Evaluation of component azimuth based on the PCA of P-wave (Black dots denote results from a single event and the red solid line indicates the average).

(1) Check and correct for the posture based on the noise data (Fig. 2a). If the seismometer is tilted, some horizontal components leak onto the vertical record and show a high level of correlation between horizontal and vertical records. Firstly, we rotate the horizontals to find the direction with maximum coherence between horizontal and vertical records. Subsequently, we calculate the transfer function between the rotated horizontal and the vertical components, which helps predict and remove the tilt noise. Generally, it is necessary to check the daily posture of the seismometer. If the tilt angle is less than 0.5, no correction is required (Bell et al., 2015).

(2) Assess the clock of seismometers by examining the teleseismic P-wave arrivals (Fig. 2b, Fig. S1). First, we obtain the initial P-wave phases of teleseismic earthquakes ($M > 6.0$) in the earthquake catalog from National Earthquake Information Center at U.S. Geological Survey (USGS-NEIC). Then, we plot the seismic waveforms ordered by the epicentral distance. If there is a systematical deviation from traveltime curves in multiple events, it indicates a clock problem with that seismometer (Z Zhang et al., 2022; Abbas et al., 2023).

(3) Check and correct the component azimuths based on teleseismic P-wave particle motion (Fig. 2c and d). To examine the component azimuth, two methods have been applied: SNR-weighted-multi-event method and principal component analysis (PCA). The first method determines the optimal component azimuth by minimizing the energy of the tangential component of teleseismic P waves, and the PCA method determines the component azimuth by calculating the eigenvalues from the covariance matrix of the horizontal components of teleseismic P-wave. We use both methods for cross-validation (Niu and Li, 2011; Wang et al., 2016).

Our analysis reveals that the majority of seismometers operated effectively, with minimal errors in posture and component azimuth. Six seismometers, however, experienced clock issues and were excluded from further analysis.

2.2. Catalog construction

We have constructed a high-precision earthquake catalog in the middle section of the ATF. The workflow is based on LOC-FLOW (Zhang et al., 2022), including phase picking, phase association, earthquake location, and magnitude computation (M_L). For the association and location of earthquakes, we utilize a modified P-wave velocity model derived from seismic refraction/wide-angle-reflection studies (Zhao et al., 2006). The S-wave velocity model is derived using empirical relationships established by Brocher (2005).

2.2.1. Phase picking

The precision of earthquake location is heavily reliant on accurate phase picking. We use PhaseNet, a deep-neural-network-based picking method modified from U-Net (Ronneberger et al., 2015), trained by about 780 000 three-component continuous waveforms (Zhu and Beroza, 2019). PhaseNet enables the prediction of P and S phase arrival times, along with their picking probabilities, from continuous three-component waveform data (Fig. 3).

During the phase picking process, we initially set a picking probability threshold of 0.1. The threshold is then iteratively adjusted based on the results of the picking and association process to ensure the identified phases are reliable. We ultimately retain *P* and *S* phases with a picking probability of no less than 0.5, as illustrated in Fig. 4.

2.2.2. Phase association

Phase association plays a crucial role in earthquake location. REAL (Rapid Earthquake Association and Location) is a three-dimensional grid-search method utilizing seismic picks, and facilitates phase association primarily by counting the number of P and S picks and secondarily by computing traveltime residuals (Zhang et al., 2019).

In this study, we employ a hierarchical search strategy. Initially, a grid search is conducted using a coarse grid covering a wider range to ascertain the approximate horizontal and depth range of earthquakes. Then, we refine our search by utilizing a finer grid to achieve more precise association and preliminary earthquake location. Finally, the

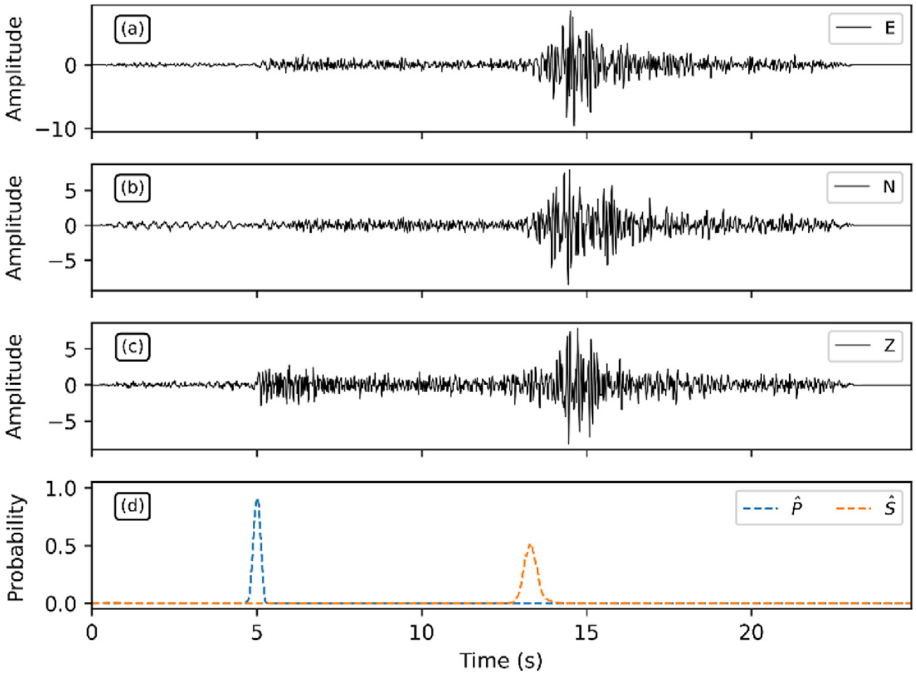

Fig. 4. A sample for phase picking. (a)–(c) Seismograms of the east, north and vertical components. (d) The converted probability for P and S picks.

searched area is set as 0.5 °× 0.5° in horizontal dimension with a grid size 0.05 °× 0.05°, and the depth range from surface to 30 km depth with an interval of 3 km. We set a strict threshold, requiring at least 5 P picks, 2 S picks, and 13 P+S picks for each earthquake. We detect 100 events with 1 903 P picks and 1 706 S picks. The hypocentral distances for most picks are within 150 km (Fig. 5).

2.2.3. *Absolute earthquake location*

HYPOINVERSE is a least-square-based locating method incorporating pick weightings based on quality, epicentral distance, and traveltime residual (Klein, 2002). For a station *i*, the difference between observed and theoretical traveltime, Δt_i , is defined as:

$$\Delta t_i = t_i - T_i(x, y, z) - t_0, \tag{1}$$

where, t_i is picker arrival, T_i is theoretical traveltime calculated by the given velocity model, and t_0 is the origin time.

The corresponding traveltime residual is:

$$\delta t_i = w_i\left(\Delta t_i - \left(\Delta t_0 + \left[\frac{\partial T_i}{\partial x}, \frac{\partial T_i}{\partial y}, \frac{\partial T_i}{\partial z}\right][\Delta x, \Delta y, \Delta z]^T\right)\right), \tag{2}$$

where, w_i is the weight of the station *i*, Δt_0 is the perturbation of the origin time, $\left[\frac{\partial T_i}{\partial x}, \frac{\partial T_i}{\partial y}, \frac{\partial T_i}{\partial z}\right]$ represents the partial derivative of the theoretical traveltime of the station *i* to the earthquake location, and $[\Delta x, \Delta y, \Delta z]^T$ is the perturbation of the earthquake location.

For an event with *n* picks, we can express (2) as a matrix equation:

$$\Delta \boldsymbol{t} - G\Delta \boldsymbol{m} = \delta t, \tag{3}$$

where $\Delta \boldsymbol{t} = [w_1\Delta t_1, \ldots, w_n\Delta t_n]$ are the differences between observed and theoretical traveltime, $\delta t = [\delta t_1, \ldots, \delta t_n]$ are residuals, $G = \begin{bmatrix} w_1 & w_1\partial T_1/\partial x & w_1\partial T_1/\partial y & w_1\partial T_1/\partial z \\ \vdots & \vdots & \vdots & \vdots \\ w_n & w_n\partial T_n/\partial x & w_n\partial T_n/\partial y & w_n\partial T_n/\partial z \end{bmatrix}$ defines a matrix of size $n \times 4$, $\Delta \boldsymbol{m} = [\Delta t_0, \Delta x, \Delta y, \Delta z]^T$ are perturbations of earthquake origin time and location. The earthquake origin time and location can be obtained by iteratively solving (3) using the least-square method.

The initial locations obtained from REAL are forwarded to HYPOINVERSE for further absolute location refinement. After further absolute location and artificial waveform check, we finally get 74 events with high precision location. The majority of events exhibit horizontal location errors within 5 km. Depth determination of the seismic source poses greater challenges, yielding relatively larger errors. Nevertheless, depth location errors for most events are also contained within 10 km. It's worth noting that certain events are impacted by insufficient station azimuthal coverage, leading to location errors exceeding 20 km, as depicted in Fig. 6.

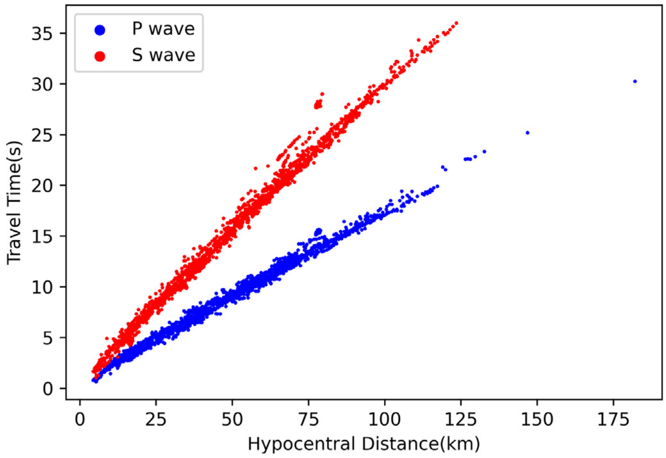

Fig. 5. Hypocentral distance and traveltime curves of *P* and *S* wave arrivals associated with REAL.

2.2.4. *Magnitude computation (M_L)*

We calculate the magnitude of the aforementioned 74 events obtained from HYPOINVERSE based on the guidelines outlined in "GB 17740–2017 General ruler for earthquake magnitude"(The General Administration of Quality Supervision, 2017). The workflow includes removing instrument response, simulating the response as a DD-1 short-period seismometer, and measuring the maximum amplitude of S waves in the horizontal records. The formula is as follows:

$$M_L = \log(A) + R(\Delta), \tag{4}$$

where, *A* represents the maximum amplitude in the horizontal records, $\mathrm{A} = (\mathrm{A_N} + \mathrm{A_E})/2$; A_N and A_E are the maximum amplitudes of S waves or Lg waves in the north and east records, measured in micrometers; Δ stands for the epicentral distance, measured in kilometers; $R(\Delta)$ represents the scaling function for local magnitude.

The magnitude is calculated as the median of the results from all stations. We get the magnitudes of earthquakes in the HYPOINVERSE catalog range between M_L -1~3, with the majority within the M_L 0–1 and M_L 1–2 (Fig. 7). This distribution is likely biased because of the difficulty in detecting earthquakes with magnitudes below M_L 0 using our observation system. Additionally, the results suggest that earthquakes of $M_\mathrm{L} >$ 2 are indeed rare during the seismic array deployment period.

2.2.5. *Match and locate*

The Match and Locate (M&L) method utilizes template events and identifies small events by stacking cross-correlograms between the waveforms of these template events and potential signals from small events in continuous waveforms across multiple stations and components. Subsequently, the detected events are located using a grid-search method (Zhang and Wen, 2015). Once an event is detected, its magnitude is computed based on the median value of the peak amplitude ratio between the detected event and the template event across all channels. The normalized cross-correlation of template events and potential events can be expressed as:

$$cc(t) = \frac{\int_{-T}^{T} u_1(\mathbf{r}_1, \tau)u_2(\mathbf{r}_2, t+\tau)\mathrm{d}\tau}{\sqrt{\int_{-T}^{T} u_1(\mathbf{r}_1, \tau)u_1(\mathbf{r}_1, t+\tau)\mathrm{d}\tau}\sqrt{\int_{-T}^{T} u_2(\mathbf{r}_2, \tau)u_2(\mathbf{r}_2, t+\tau)\mathrm{d}\tau}}, \tag{5}$$

where $u_1(\mathbf{r}_1, \tau)$ and $\mathbf{r}_1$ indicate waveform of the template event and distance vector between template event and station; $u_2(\mathbf{r}_2, t+\tau)$ and $\mathbf{r}_2$ indicate waveform of the potential event and distance vector between potential event and station; *T* corresponds to the length of the time window of the reference phase.

The M&L method primarily detects events by evaluating the similarity of the source time function and radiation pattern between events. We need to ensure that $\mathbf{r}_1$ and $\mathbf{r}_2$ areclose enough to remove the effects of attenuation and Green's function. We select 40 seismic events from the HYPOINVERSE catalog as template events based on criteria including horizontal and vertical location errors not exceeding 5 km, recorded by more than 5 stations, and possessing signal-to-noise ratios greater than 2. These template waveforms containing *S* wave are applied running cross-correlation with the continuous waveform at each station and component. Due to the absence of nearby stations and the significant trade-off between depth and origin time, constraining earthquake depth accurately is challenging (Billings et al., 1994; Zhang et al., 2014). Hence, we fix the depth to be the same as the template and solely searched for potential horizontal locations, within a mesh size of 0.2° × 0.2° and a searching interval of 0.02° × 0.02°.

The filtering frequency band is a critical parameter for template matching. In our approach, we utilized the short-time Fourier transform (STFT) to conduct a time-frequency analysis of template events (Fig. 8), allowing us to assess their energy distribution and determine the

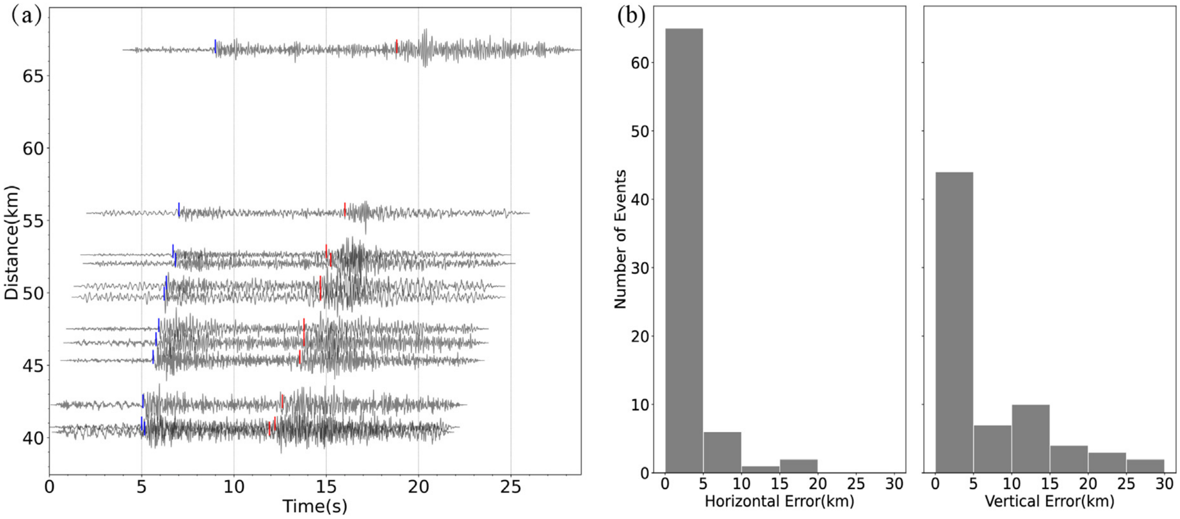

Fig. 6. Location and quality analysis from HYPOINVERSE. (a) Vertical waveforms aligned by epicentral distance (Event: 2021-09-27T19:28:05.480UTC, M_L 0.94). The blue and red solid lines denote P and S picks, respectively. (b) Histograms for distribution of horizontal and depth location errors.

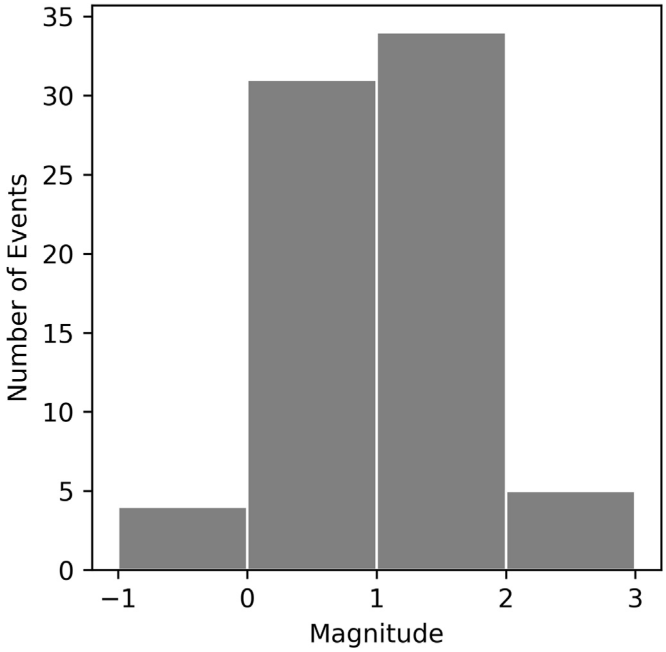

Fig. 7. Histograms for distribution of magnitudes (M_L) in HYPOINVERSE catalog.

appropriate filtering frequency band. For this study, we use a filtering frequency band of 2–20 Hz.

To ensure the reliability of the detected events, we set minimum criteria for the correlation coefficient (CC) and median deviation multiples (N*MAD). We preserve only those events with a CC of 0.3 or higher and an N*MAD of 10 or higher (Fig. 9). Subsequently, after manual verification, we identify 233 earthquakes, a significant increase compared to the 6 earthquakes in the routine catalog during the deployment period.

3. Results and discussions

As shown in Fig. 10, the newly detected earthquakes are predominantly located within a 150 km radius of the array, limited by the arrangement of short-period stations, sparse coverage of permanent stations, and weak seismic activity in the area. When compared to the routine catalog (which contains 6 earthquakes within our detected radius), we find that 5 among them matched with events in the HYPOINVERSE catalog. The remaining 1 earthquake is screened out by REAL due to insufficient P and S picks.

Because the earthquake depth is fixed to be the same as the template, only the horizontal locations of the M&L catalog are displayed (Fig. 11). The M&L method successfully detect a greater number of small-magnitude events, including those with magnitudes falling within the range M_L 0–1 and $M_L < 0$.

From Figs. 10 and 11, it is apparent that the newly detected earthquakes are clustered around 90°E along the ATF. Moreover, several earthquakes with larger magnitudes were occurred along the southern secondary faults, similar to the distribution of historical earthquakes (Fig. 12). Based on the focal mechanisms of historical earthquakes (Fig. 12), those occurring along the ATF predominantly exhibit strike-slip mechanisms, whereas those located along the southern secondary faults display thrust mechanisms. This seismic activity in the middle section of the ATF is likely attributed to the northeastward transpressional motion of the Qinghai-Xizang Plateau block at the western margin of the Qaidam Basin (Chen et al., 1999; Cheng et al., 2021).

4. Conclusions

We construct a high-precision catalog with 233 (M_L -1-3) earthquakes in the middle section of ATF from September 17 to November 23, 2021. Our approach of combining dense array and machine learning method has proven effective in improving the completeness of the local catalog, particularly in fault zones with weak seismicity. Integrating historical earthquake data, focal mechanism solutions, and local fault structure, we find that seismic events are mainly along the ATF and on the southern secondary faults. Earthquakes along the ATF mostly exhibit strike-slip focal mechanisms, whereas earthquakes near southern secondary faults behave as thrust faulting. The overall seismicity may be related to the northeastward transpressional motion of the Qinghai-Xizang Plateau block on the western margin of the Qaidam Basin. Given the seismicity distribution, it is crucial to monitor the fault activity along the ATF and its southern branch faults to mitigate potential seismic hazards.

Data and resources

Continuous waveform data for 3 permanent stations and routine catalog were downloaded from the International Earthquake Science

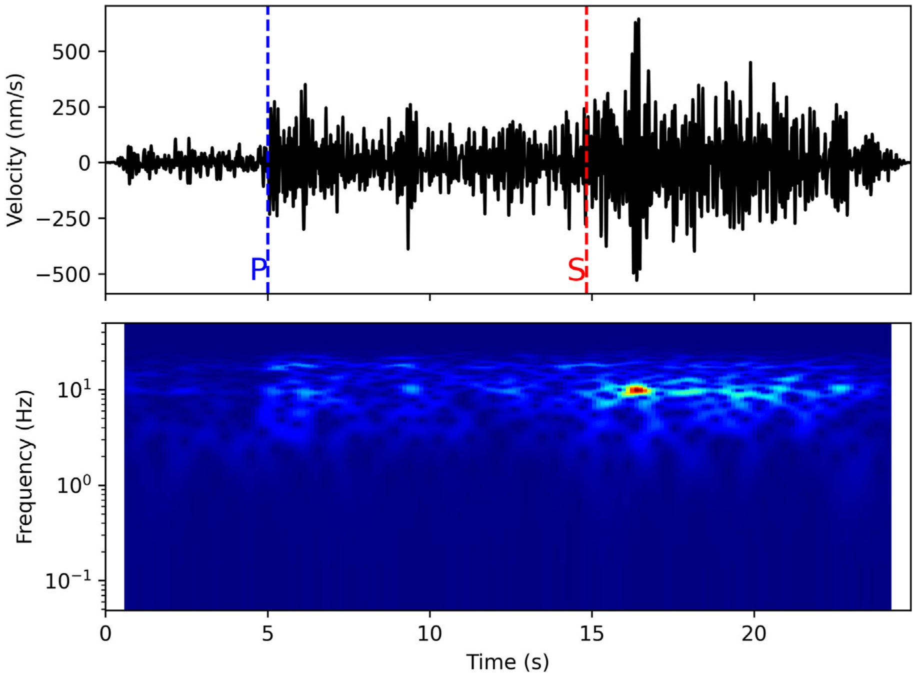

Fig. 8. Time-frequency analysis of seismic event waveform. (a) An example of seismic waveform. The blue dashed and red dashed lines mark the P and S arrivals, respectively. (b) The corresponding spectrogram.

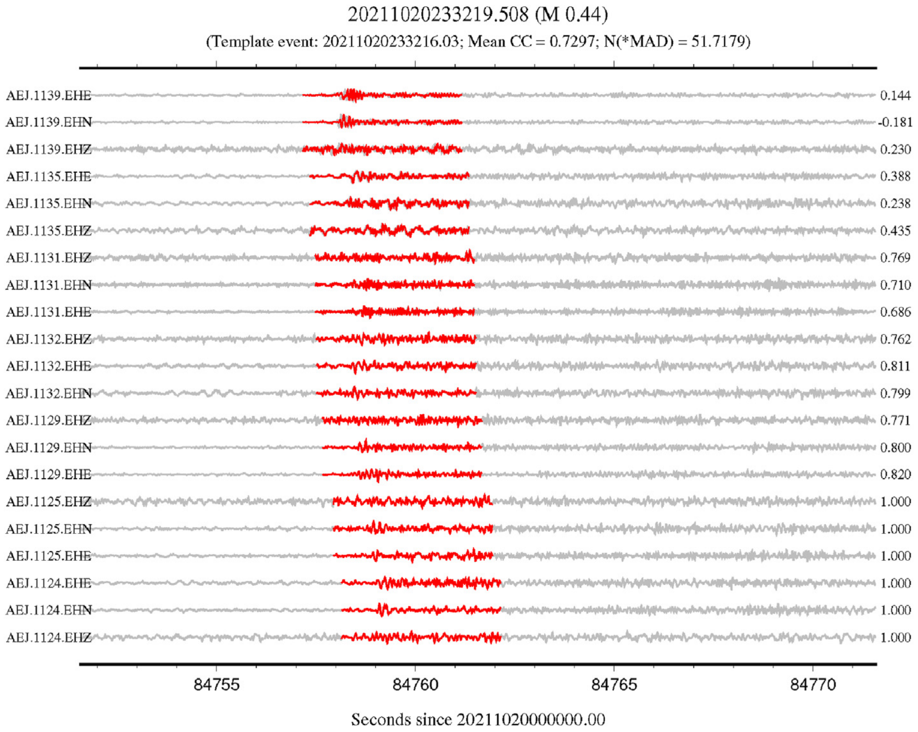

Fig. 9. An example comparison of template seismograms for 2021-10-20T233216.03 (M_L 0.63) (red) with a portion of the seismic signal detected in the continuous waveform data for the event 2021-10-20T23:32:19.508 (M_L 0.44). The left side marks the station and component of the waveform, while the right side marks the correlation coefficient.

Data Center at http://www.esdc.ac.cn/. Focal mechanism solutions were downloaded from Global Centroid-Moment-Tensor at https://www.globalcmt.org/. LOCFLOW can be found at https://github.com/Dal-mzhang/LOC-FLOW. PhaseNet was downloaded at https://github.com/AI4EPS/PhaseNet. REAL was downloaded at https://github.com/Dal-mzhang/REAL. HYPOINVERSE was downloaded at https://faldersons.net/Software/Hypoinverse/Hypoinverse.html. M&L was downloaded at https://github.com/Dal-mzhang/MatchLocate2.

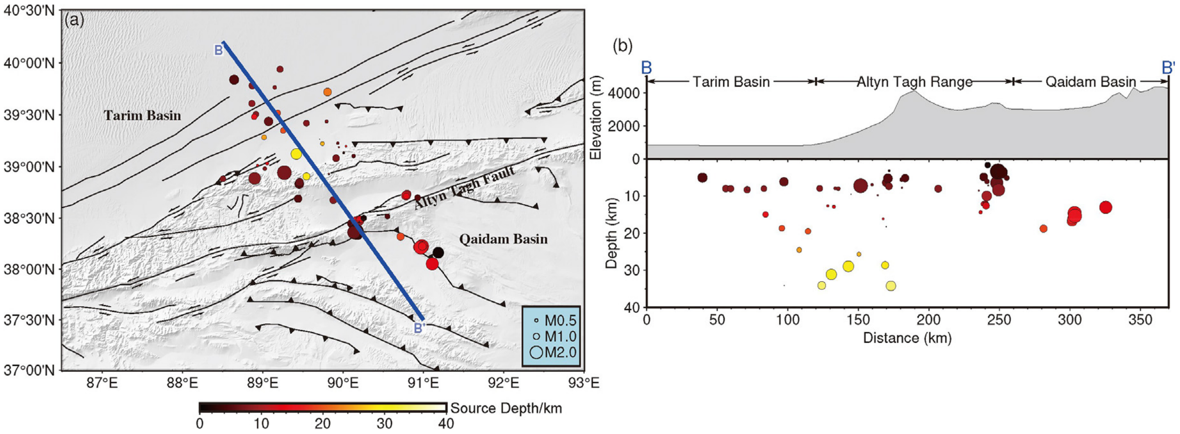

Fig. 10. Earthquake location of HYPOINVERSE catalog. (a) Earthquake locations in map view. (b) Earthquake locations along profile BB '. Earthquakes are scaled by the magnitude and color-coded by the source depth.

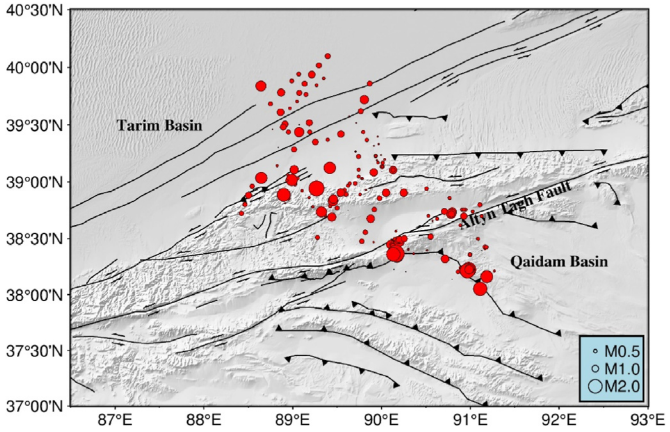

Fig. 11. Match and Locate catalog. The red dots denote the earthquakes and their size indicates the magnitude (M_L).

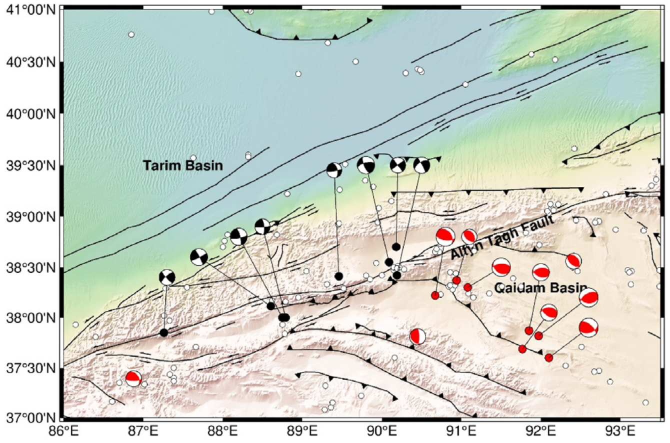

Fig. 12. Historical earthquakes and focal mechanism in the middle section of ATF. White dots show $M>3$ earthquakes from 2007-2022 from the International Earthquake Science Data Center. The black and red focal mechanisms show the strike-slip and thrust events from the GCMT catalog from 1970 to 2022, respectively.

Declaration of competing interest

The authors declare that they have no known competing financial interests or personal relationships that could have appeared to influence the work reported in this paper. The corresponding author Tao Xu is an editorial board member for *Earthquake Research Advances* and was not involved in the editorial review or the decision to publish this article. All authors declare that there are no competing interests.

Acknowledgments

The authors thank Prof. Gaohua Zhu from the Institute of Oceanology, Chinese Academy of Sciences for her constructive advice. We thank the two anonymous reviewers for their comments, which greatly improved the article. This work was supported by the Second Tibetan Plateau Scientific Expedition and Research Program (STEP, 2019QZKK0701-02) and the National Natural Science Foundation of China (Grant 42104102 and 42130807).

Appendix A. Supplementary data

Supplementary data to this article can be found online at https://doi.org/10.1016/j.eqrea.2024.100308.

References

Abbas, A., Zhu, G., Zi, J., et al., 2023. Evaluating and correcting short-term clock drift in data from temporary seismic deployments. Earthquake Research Advances 3 (2), 100199.

Ammirati, J.B., Villaseñor, A., Chevrot, S., et al., 2022. Automated earthquake detection and local travel time tomography in the south-central andes (32–35° S): implications for regional tectonics. J. Geophys. Res. Solid Earth 127 (4), e2022JB024097.

Bell, S.W., Forsyth, D.W., Ruan, Y., 2015. Removing noise from the vertical component records of ocean-bottom seismometers: results from year one of the Cascadia Initiative. Bull. Seismol. Soc. Am. 105 (1), 300–313.

Bendick, R., Bilham, R., Freymueller, J., et al., 2000. Geodetic evidence for a low slip rate in the Altyn Tagh fault system. Nature 404 (6773), 69–72.

Billings, S.D., Kennett, B.L.N., Sambridge, M.S., 1994. Hypocentre location: genetic algorithms incorporating problem-specific information. Geophys. J. Int. 118 (3), 693–706.

Brocher, T.M., 2005. Empirical relations between elastic wavespeeds and density in the Earth's crust. Bull. Seismol. Soc. Am. 95 (6), 2081–2092.

Chen, W.P., Chen, C.Y., Nábelek, J.L., 1999. Present-day deformation of the Qaidam basin with implications for intra-continental tectonics. Tectonophysics 305 (1–3), 165–181.

Cheng, F., Jolivet, M., Guo, Z., et al., 2021. Cenozoic evolution of the Qaidam basin and implications for the growth of the northern Tibetan plateau: a review. Earth Sci. Rev. 220, 103730.

Daniels, C., Peng, Z., 2023. A 15-year-Long catalog of seismicity in the Eastern Tennessee Seismic Zone (ETSZ) using matched filter detection. Earthquake Research Advances 3 (1), 100198.

Deng, Q.D., 2007. China's Active Tectonic Map (1:4 Million) [M]. Earthquake Press.

Elliott, J.R., Biggs, J., Parsons, B., et al., 2008. InSAR slip rate determination on the Altyn Tagh Fault, northern Tibet, in the presence of topographically correlated atmospheric delays. Geophys. Res. Lett. 35 (12).

Jiang, C., Zhang, P., White, M.C.A., et al., 2022. A detailed earthquake catalog for Banda Arc–Australian plate collision zone using machine-learning phase picker and an automated workflow. The Seismic Record 2 (1), 1–10.

Klein, F.W., 2002. User's Guide to HYPOINVERSE-2000, a Fortran Program to Solve for Earthquake Locations and magnitudes[R]. US Geological Survey.

Li, Y., Shan, X., Qu, C., et al., 2018. Crustal deformation of the Altyn Tagh fault based on GPS. J. Geophys. Res. Solid Earth 123 (11), 10309–10322.

Liu, M., Zhang, M., Zhu, W., et al., 2020. Rapid characterization of the July 2019 Ridgecrest, California, earthquake sequence from raw seismic data using machine-learning phase picker. Geophys. Res. Lett. 47 (4), e2019GL086189.

Molnar, P., Tapponnier, P., 1975. Cenozoic Tectonics of Asia: effects of a Continental Collision: features of recent continental tectonics in Asia can be interpreted as results of the India-Eurasia collision. Science 189 (4201), 419–426.

Mousavi, S.M., Ellsworth, W.L., Zhu, W., et al., 2020. Earthquake transformer—an attentive deep-learning model for simultaneous earthquake detection and phase picking. Nat. Commun. 11 (1), 3952.

Mousavi, S.M., Sheng, Y., Zhu, W., et al., 2019. STanford EArthquake Dataset (STEAD): a global data set of seismic signals for AI. IEEE Access 7, 179464–179476.

Niu, F., Li, J., 2011. Component azimuths of the CEArray stations estimated from P-wave particle motion. Earthq. Sci. 24, 3–13.

Ou, Q., Kulikova, G., Yu, J., et al., 2020. Magnitude of the 1920 Haiyuan earthquake reestimated using seismological and geomorphological methods. J. Geophys. Res. Solid Earth 125 (8), e2019JB019244.

Park, Y., Mousavi, S.M., Zhu, W., et al., 2020. Machine-learning-based analysis of the Guy-Greenbrier, Arkansas earthquakes: a tale of two sequences. Geophys. Res. Lett. 47 (6), e2020GL087032.

Peng, Z., Zhao, P., 2009. Migration of early aftershocks following the 2004 Parkfield earthquake. Nat. Geosci. 2 (12), 877–881.

Pu, X., Wang, L., Wang, P., et al., 2022. The response law of far-field seismic ground motion of the Wenchuan earthquake and its damaging mechanism in the Loess Plateau. Earthquake Research Advances 2 (3), 100114.

Robinson, D.P., Brough, C., Das, S., 2006. The Mw 7.8, 2001 Kunlunshan earthquake: extreme rupture speed variability and effect of fault geometry. J. Geophys. Res. Solid Earth 111 (B8).

Ronneberger, O., Fischer, P., Brox, T., 2015. U-Net: convolutional networks for biomedical image segmentation. Miccai 9351, 234–241.

Shelly, D.R., Beroza, G.C., Ide, S., 2007. Non-volcanic tremor and low-frequency earthquake swarms. Nature 446 (7133), 305–307.

Shelly, D.R., Ellsworth, W.L., Hill, D.P., 2016. Fluid-faulting evolution in high definition: connecting fault structure and frequency-magnitude variations during the 2014 Long Valley Caldera, California, earthquake swarm. J. Geophys. Res. Solid Earth 121 (3), 1776–1795.

Shen, Z.K., Sun, J., Zhang, P., et al., 2009. Slip maxima at fault junctions and rupturing of barriers during the 2008 Wenchuan earthquake. Nat. Geosci. 2 (10), 718–724.

Shen, Z.K., Wang, M., Li, Y., et al., 2001. Crustal deformation along the Altyn Tagh fault system, western China, from GPS. J. Geophys. Res. Solid Earth 106 (B12), 30607–30621.

Stewart, S.W., 1977. Real-time detection and location of local seismic events in central California. Bull. Seismol. Soc. Am. 67 (2), 433–452.

Styron, R., Taylor, M., Okoronkwo, K., 2010. Database of active structures from the Indo-Asian collision. Eos, Transactions American Geophysical Union 91 (20), 181–182.

Su, J.B., Liu, M., Zhang, Y.P., et al., 2021. High resolution earthquake catalog building for the 21 May 2021 Yangbi, Yunnan, M_S 6.4 earthquake sequence using deep-learning phase picker. Chin. J. Geophys. 64 (8), 2647–2656.

Tapponnier, P., Zhiqin, X., Roger, F., et al., 2001. Oblique stepwise rise and growth of the Tibet Plateau. Science 294 (5547), 1671–1677.

The General Administration of Quality Supervision, 2017. Inspection and Quarantine of the People's Republic of China, and the Standardization Administration of China. GB 17740-2017 Specification for Earthquake Magnitude [S]. China Standard Press, Beijing.

Waldhauser, F., Ellsworth, W.L., 2002. Fault structure and mechanics of the Hayward fault, California, from double-difference earthquake locations. J. Geophys. Res. Solid Earth 107 (B3). ESE 3-1-ESE 3-15.

Wallace, K., Yin, G., Bilham, R., 2004. Inescapable slow slip on the Altyn Tagh fault. Geophys. Res. Lett. 31 (9).

Wang, J., Xiao, Z., Liu, C., et al., 2019. Deep learning for picking seismic arrival times. J. Geophys. Res. Solid Earth 124 (7), 6612–6624.

Wang, K., Zhang, J., Zhang, J., et al., 2023. Monitoring seismicity in the southern Sichuan Basin using a machine learning workflow. Earthquake Research Advances, 100241.

Wang, M., Shen, Z.K., 2020. Present-day crustal deformation of continental China derived from GPS and its tectonic implications. J. Geophys. Res. Solid Earth 125 (2), e2019JB018774.

Wang, R., Yang, D., Chen, Y., et al., 2023. Lighting up a 1 km fault near a hydraulic fracturing well using a machine learning-based picker. Seismol Res. Lett.

Wang, W., Fang, L., Wu, J., et al., 2021. Aftershock sequence relocation of the 2021 M_S 7.4 Maduo earthquake, Qinghai, China. Sci. China Earth Sci. 64, 1371–1380.

Wang, X., Chen, Q.F., Li, J., et al., 2016. Seismic sensor misorientation measurement using P-wave particle motion: an application to the NECsaids array. Seismol Res. Lett. 87 (4), 901–911.

Wen, X.X., Shen, X.Z., Zhou, Q.M., 2022. Study on the characters of the aftershocks of Beiliu 5.2 earthquake using machine learning method and dense nodal seismic array. Chin. J. Geophys. 65 (9), 3297–3308.

Wilding, J.D., Zhu, W., Ross, Z.E., et al., 2023. The magmatic web beneath Hawai ‘i. Science 379 (6631), 462–468.

Wu, C., Xu, T., Tian, X., et al., 2024. Underthrusting of Tarim lower crust beneath the Tibetan Plateau revealed by receiver function imaging. Geophys. Res. Lett. 51.

Wu, X., Huang, S., Xiao, Z., et al., 2022. Building precise local submarine earthquake catalogs via a deep-learning-empowered workflow and its application to the challenger deep. Front. Earth Sci. 10, 34.

Xie, T., Xu, T., Yang, Y., et al., 2023. Observation of higher-mode Rayleigh waves from ambient noise in the Tarim Basin, China. Seismol Res. Lett. 94 (4), 1848–1859.

Yang, H., Zhu, L., Chu, R., 2009. Fault-plane determination of the 18 April 2008 Mount Carmel, Illinois, earthquake by detecting and relocating aftershocks. Bull. Seismol. Soc. Am. 99 (6), 3413–3420.

Xu, Z.Q., Li, H.B., Tang, Z.M., et al., 2011. The transformation of the terrain structures of the Tibet Plateau through large-scale strike-slip faults. Acta Petrol. Sin. 27 (11), 3157–3170.

Yang, T.W., Xu, Y., Nan, F.Z., et al., 2023. Construction and application of preprocessing technology for passive source ocean bottom seismometer data. Chin. J. Geophys. 66 (2), 746–759.

Yin, A., Rumelhart, P.E., Butler, R., et al., 2002. Tectonic history of the Altyn Tagh fault system in northern Tibet inferred from Cenozoic sedimentation. Geol. Soc. Am. Bull. 114 (10), 1257–1295.

Yuan, Z., Liu-Zeng, J., Li, X., et al., 2021. Detailed mapping of the surface rupture of the 12 february 2014 yutian *Ms* 7.3 earthquake, Altyn Tagh Fault, Xinjiang, China. Sci. China Earth Sci. 64, 127–147.

Yuan, Z., Liu-Zeng, J., Wang, W., et al., 2018. A 6000-year-long paleoseismologic record of earthquakes along the Xorkoli section of the Altyn Tagh fault, China. Earth Planet Sci. Lett. 497, 193–203.

Zhang, M., Ellsworth, W.L., Beroza, G.C., 2019. Rapid earthquake association and location. Seismol Res. Lett. 90 (6), 2276–2284.

Zhang, M., Liu, M., Feng, T., et al., 2022. LOC-FLOW: an end-to-end machine learning-based high-precision earthquake location workflow. Seismol Res. Lett. 93 (5), 2426–2438.

Zhang, M., Tian, D., Wen, L., 2014. A new method for earthquake depth determination: stacking multiple-station autocorrelograms. Geophys. J. Int. 197 (2), 1107–1116.

Zhang, M., Wen, L., 2015. An effective method for small event detection: match and locate (M&L). Geophys. J. Int. 200 (3), 1523–1537.

Zhang, P.Z., Molnar, P., Xu, X., 2007. Late Quaternary and present-day rates of slip along the Altyn Tagh Fault, northern margin of the Tibetan Plateau. Tectonics 26 (5).

Zhang, Z., Deng, Y., Qiu, H., et al., 2022. High-Resolution imaging of fault zone structure along the creeping section of the Haiyuan Fault, NE tibet, from data recorded by dense seismic arrays. J. Geophys. Res. Solid Earth 127 (9), e2022JB024468.

Zhao, J., Mooney, W.D., Zhang, X., et al., 2006. Crustal structure across the Altyn Tagh Range at the northern margin of the Tibetan plateau and tectonic implications. Earth Planet Sci. Lett. 241 (3–4), 804–814.

Zhao, M., Tang, L., Chen, S., et al., 2021. Machine learning based automatic foreshock catalog building for the 2019 M_S 6.0 Changning, Sichuan earthquake. Chin. J. Geophys. 64 (1), 54–66.

Zhao, M., Xiao, Z., Chen, S., et al., 2022. DiTing: a large-scale Chinese seismic benchmark dataset for artificial intelligence in seismology. Earthq. Sci. 35, 1–11.

Zhou, Y., Ghosh, A., Fang, L., et al., 2021. A high-resolution seismic catalog for the 2021 M_S 6. 4/M_W 6. 1 Yangbi earthquake sequence, Yunnan, China: application of AI picker and matched filter. Earthq. Sci. 34 (5), 390–398.

Zhou, Y., Yue, H., Fang, L., et al., 2022a. An earthquake detection and location architecture for continuous seismograms: phase picking, association, location, and matched filter (PALM). Seismol Res. Lett. 93 (1), 413–425.

Zhou, Y., Yue, H., Zhou, S., et al., 2022b. Microseismicity along Xiaojiang fault zone (southeastern Tibetan plateau) and the characterization of interseismic fault behavior. Tectonophysics 833, 229364.

Zhu, W., Beroza, G.C., 2019. PhaseNet: a deep-neural-network-based seismic arrival-time picking method. Geophys. J. Int. 216 (1), 261–273.

Zhu, W., Hou, A.B., Yang, R., et al., 2023. QuakeFlow: a scalable machine-learning-based earthquake monitoring workflow with cloud computing. Geophys. J. Int. 232 (1), 684–693.

Zuo, K., Zhao, C., 2023. Seismicity and seismogenic mechanism of the M_S 6.0 Luxian earthquake on September 16, 2021. Earthquake Research Advances 3 (4), 100253.